Enhanced-resolution lidar

Christophe F. Bas, Timothy J. Kane, and Christopher S. Ruf

The Communications and Space Sciences Laboratory, The Pennsylvania State University, 316 Electrical Engineering East, University Park, Pennsylvania 16802-2707

Received March 28, 1996; revised manuscript received October 31, 1996; accepted November 8, 1996

To retrieve a high-resolution vector signal from a set of measured low-resolution vector signals, we deliberately delayed the synchronization between the transmitter and the receiver of a pulsed laser radar (lidar). Once several range-shifted low-resolution vector signals had been obtained, we independently applied a regularization method and the singular-value-decomposition method to restore high-resolution characteristics. The former approach remains preferable when the signal-to-noise ratio is low, whereas the latter provides results similar to those of the former, but with lesser effort, as the signal-to-noise ratio becomes high. © 1997 Optical Society of America [S0740-3232(97)00205-6]

1. INTRODUCTION

The field of image processing has shown that blurred, noisy, and randomly space-shifted series of images could be satisfactorily recovered by using methods either in the space domain or in the wave-number domain.[1] Successful restoration of this inverse problem can be performed through regularization techniques,[2,3] which require some statistical knowledge of the image and its associated noise. The Wiener filter[4–7] is a particular type of regularization filter.

Instead of taking a bidimensional image, pulsed laser radars (lidars) capture a vector signal of the environment with each shot. Assuming that this environment remains static (often referred to as frozen), a delay of the synchronization between the transmitter and the receiver provides information complementary to that of the initial pulse. The low-resolution vector signals obtained from the emission of several desynchronized pulses form a complete set of measurements whose inverse reconstructs a high-resolution vector signal. When the effect of noise is important, better results are provided by the regularization method than by the unconstrained restoration techniques. However, when the effect of noise is small, unconstrained restoration methods deliver satisfactory results while diminishing the complexity of the calculations.

The compromise among the validity of the static-environment supposition, the high frequencies of interest, and the maximum sampling rate obtainable with available devices determines the optimum number of pulses necessary to make a complete set of measurements.

Section 2 elaborates on the proposed technique to retrieve high-resolution signals and Section 3 sets up a degradation model. Section 4 focuses on the restoration methods, Section 5 provides examples, and Section 6 concludes this paper.

2. TECHNIQUE

Lidars[8] include two entities: a transmitter and a receiver. The transmitter sends a narrow pulse that travels at almost $c \approx 3 \times 10^8$ m/s. Every location illuminated by the pulse scatters toward the receiver some information that is processed and delivered as a discrete signal of finite length: a low-resolution signal of dimension $1 \times M$. The system requires a dwell-time period of T seconds per element (also called bin, channel, or pixel). Synchronization between the two entities ensures that the location of the source of information is known at all times within $T \times c$ meters. Our objective is to provide a high-resolution signal whose dimension is $1 \times (MN + N - 1)$, where N is the spatial amplification factor, reducing the imprecision to within $T \times c/N$ m.

Toward this aim, and toward the construction of one complete set of measurements, N periodic pulses need to be transmitted, each of which is shifted in time by T/N with respect to the actual synchronization instant of the previous pulse, as shown Fig. 1. The consequence of this technique is, as illustrated in Fig. 2, to allow for the use of the same degradation model for either photon-counting or low-pass-filter-equipped sampling devices (in which case the degradation matrix $\mathbf{H}_{\mathrm{NTI}}$ defined later needs to be divided by the period T).

3. DEGRADATION MODEL

The degradation model is expressed as

$$\mathbf{z}_{\mathrm{NTI}} = \mathbf{y}_{\mathrm{NTI}} + \mathbf{n}, \tag{1}$$

with

$$\mathbf{y}_{\mathrm{NTI}} = \mathbf{H}_{\mathrm{NTI}}\mathbf{x}^t, \tag{2}$$

where $\mathbf{y}_{\mathrm{NTI}} = [\mathbf{y}_1 \quad \mathbf{y}_2 \quad \mathbf{y}_3 \cdots \mathbf{y}_M]^t$ is the column vector made of the low-resolution vector signals obtained by successive pulses; $\mathbf{x}$ is the high-resolution vector signal that we hope to retrieve; $\mathbf{n}$ is the contribution of noise throughout the system and modeled as additive, white, and Gaussian with zero mean; and $\mathbf{H}_{\mathrm{NTI}}$ is the degradation matrix whose dimension is $(MN) \times (MN + N - 1)$, whose structure follows from the technique used therein:

 © 1997 Optical Society of America

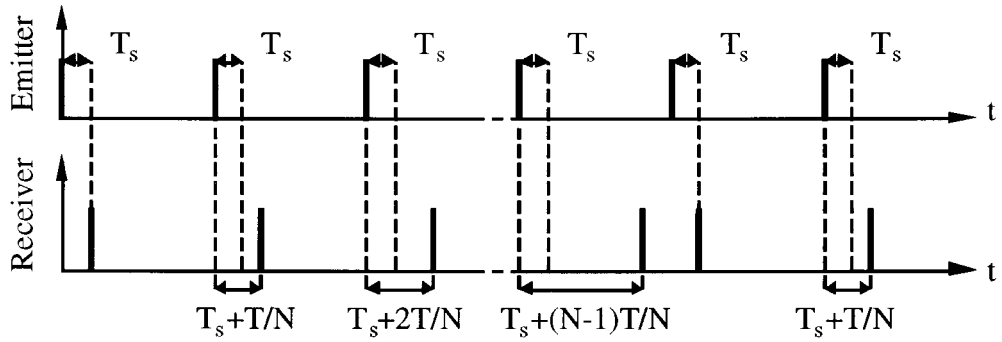

Fig. 1. Illustration of the technique used to obtain a high-resolution vector signal from N low-resolution vector signals. The periodic thick lines at the emitter represent the time of emission of a pulse, whereas the actual recording time at the receiver begins at $T_s + \langle i \rangle_N \times (T/N)$, where T_s is the nominal synchronization time, i is a natural number, and $\langle i \rangle_N$ is the value of i modulo N.

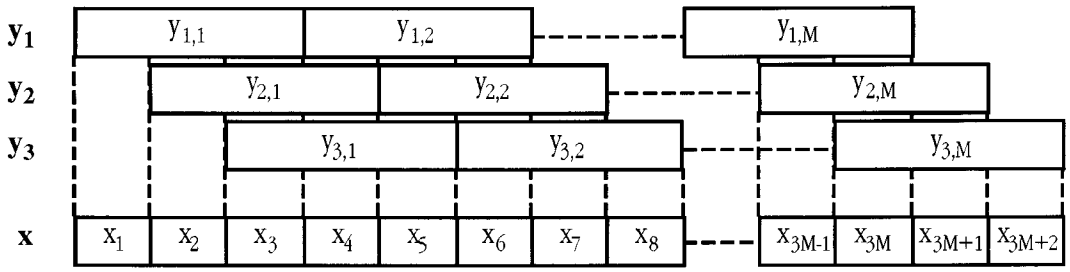

Fig. 2. When three pulses are sent ($N = 3$), the corresponding three low-resolution vector signals ($\mathbf{y}_1$, $\mathbf{y}_2$, and $\mathbf{y}_3$) form a complete set of measurements. All low-resolution vector signals are related to the high-resolution vector signal $\mathbf{x}$ through the time-shift technique.

$$\mathbf{H}_{\mathrm{NTI}} = \begin{bmatrix} 1 & 1 & \cdots & 1 & 0 & 0 & \cdots & 0 & 0 & 0 & \cdots & 0 & 0 & 0 & \cdots & 0 & 0 & 0 \\ 0 & 0 & \cdots & 0 & 1 & 1 & \cdots & 1 & 0 & 0 & \cdots & 0 & 0 & 0 & \cdots & 0 & 0 & 0 \\ \vdots & \vdots & & \vdots & \vdots & \vdots & & \vdots & \vdots & \vdots & & \vdots & \vdots & \vdots & & \vdots & \vdots & \vdots \\ 0 & 0 & \cdots & 0 & 0 & 0 & \cdots & 0 & 0 & 0 & \cdots & 1 & 1 & 0 & \cdots & 0 & 0 & 0 \\ 0 & 1 & \cdots & 1 & 1 & 0 & \cdots & 0 & 0 & 0 & \cdots & 0 & 0 & 0 & \cdots & 0 & 0 & 0 \\ 0 & 0 & \cdots & 0 & 0 & 1 & \cdots & 1 & 1 & 0 & \cdots & 0 & 0 & 0 & \cdots & 0 & 0 & 0 \\ \vdots & \vdots & & \vdots & \vdots & \vdots & & \vdots & \vdots & \vdots & & \vdots & \vdots & \vdots & & \vdots & \vdots & \vdots \\ 0 & 0 & \cdots & 0 & 0 & 0 & \cdots & 0 & 0 & 0 & \cdots & 1 & 1 & 1 & \cdots & 0 & 0 & 0 \\ 0 & 0 & \cdots & 1 & 1 & 1 & \cdots & 0 & 0 & 0 & \cdots & 0 & 0 & 0 & \cdots & 0 & 0 & 0 \\ 0 & 0 & \cdots & 0 & 0 & 0 & \cdots & 1 & 1 & 1 & \cdots & 0 & 0 & 0 & \cdots & 0 & 0 & 0 \\ \vdots & \vdots & & \vdots & \vdots & \vdots & & \vdots & \vdots & \vdots & & \vdots & \vdots & \vdots & & \vdots & \vdots & \vdots \\ 0 & 0 & \cdots & 0 & 0 & 0 & \cdots & 0 & 0 & 0 & \cdots & 0 & 0 & 0 & \cdots & 1 & 1 & 1 \end{bmatrix}. \tag{3}$$

Although $\mathbf{H}_{\mathrm{NTI}}$ does not display the property of time invariance (which is at the origin of its subscript), it is possible to restructure the matrix so that it does. We shall call this new matrix $\mathbf{H}_{\mathrm{TI}}$, which is obtained by writing $\mathbf{y}_{\mathrm{TI}} = \mathbf{H}_{\mathrm{TI}}\mathbf{x}^t$, where (see Fig. 2)

$$\mathbf{H}_{\mathrm{TI}} = \begin{bmatrix} 1 & 1 & 1 & \cdots & 1 & 0 & 0 & 0 & \cdots & 0 & 0 & 0 & 0 & \cdots & 0 \\ 0 & 1 & 1 & \cdots & 1 & 1 & 0 & 0 & \cdots & 0 & 0 & 0 & 0 & \cdots & 0 \\ 0 & 0 & 1 & \cdots & 1 & 1 & 1 & 0 & \cdots & 0 & 0 & 0 & 0 & \cdots & 0 \\ \vdots & \vdots & \vdots & & \vdots & \vdots & \vdots & \vdots & & \vdots & \vdots & \vdots & \vdots & & \vdots \\ 0 & 0 & 0 & \cdots & 0 & 0 & 0 & 0 & \cdots & 0 & 1 & 1 & 1 & \cdots & 1 \end{bmatrix} \tag{4}$$

and $\mathbf{y}_{\mathrm{TI}} = [y_{1,1} \quad y_{2,1} \quad y_{3,1} \quad \cdots \quad y_{N,1} \quad y_{1,2} \quad \cdots \quad y_{N,2} \quad y_{1,3} \quad \cdots \quad y_{1,M} \quad y_{2,M} \quad \cdots \quad y_{1,M}]^t$.

The previous result is generalized as $y_{\mathrm{TI}}(k) = h_{\mathrm{TI}}(k) * x(k)$, where $*$ denotes the convolution operator and

$$h_{\mathrm{TI}}(k) = \begin{cases} 1 & \text{for } k = 0, 1, 2 \ldots N-1 \\ 0 & \text{otherwise} \end{cases}, \tag{5}$$

whose frequency domain counterpart is

$$H_{\mathrm{TI}}[\exp(j\omega T)] = \exp[-j\omega T(N-1)/2]\,\frac{\sin(\omega TN/2)}{\sin(\omega T/2)}. \tag{6}$$

We conclude that the recovery (which makes use of $\mathbf{H}_{\mathrm{NTI}}$) will not be successful for frequencies at and around those for which $H_{\mathrm{TI}}[\exp(j\omega T)] = 0$. Hence one must strongly consider the range of frequencies of interest before choosing N.

4. RESTORATION

We seek a way to compute $\hat{\mathbf{x}}^t_{\mathrm{NTI}} = \mathbf{H}^{-1}\mathbf{z}_{\mathrm{NTI}}$ while controlling the effect of the noise in our ill-posed inversion. $\hat{\mathbf{x}}$ denotes one of the possible high-resolution vector signals. The expression for $\mathbf{H}^{-1}$ is the topic of this section. Two solutions are suggested, the selection of which is motivated by the value of the signal-to-noise ratio (SNR_z) estimated from the low-resolution vector signals.

In the regularized underconstrained inverse (RUI) approach, we restrict ourselves to the minimization of the following function:

$$\|\mathbf{y} - \mathbf{H}_{\mathrm{NTI}}\mathbf{x}\|^2 + \gamma\|\mathbf{x}\|^2, \tag{7}$$

where small values for γ give an emphasis to the data points, whereas large values promote a smooth result for the estimation of the high-resolution vector signal.[9] The resulting solution[2,3] is found to be

$$\mathbf{H}^{-1} \equiv \mathbf{H}^t_{\mathrm{NTI}}(\mathbf{H}_{\mathrm{NTI}}\mathbf{H}^t_{\mathrm{NTI}} + \gamma\mathbf{I})^{-1}, \tag{8}$$

where $\gamma = C/\mathrm{SNR}_z$ and $\mathbf{I}$ is the identity matrix. The real constant C was determined for the simulated signals of Section 5 by selecting the C that minimized the mean square error (MSE) between the known low-resolution vector signal $\mathbf{y}$ and $\mathbf{H}_{\mathrm{NTI}}\hat{\mathbf{x}}$, the degraded version of the restored high-resolution vector signal, for which γ is used. Wahba[10] suggested practical means to evaluate γ from noisy data.

If the effect of the noise is small, γ in Eq. (8) becomes so small that it is tempting to write $\mathbf{H}^{-1} \equiv \mathbf{H}^t_{\mathrm{NTI}} \times (\mathbf{H}_{\mathrm{NTI}}\mathbf{H}^t_{\mathrm{NTI}})^{-1}$, the underconstrained inverse.[6,11] Nonetheless, this last equation and $\mathbf{H}^{-1} = \mathbf{H}^{-1}_{\mathrm{NTI}}$, solved through the singular value decomposition (SVD) method, lead to the same results. SVD has been chosen over other unconstrained methods because of its simplicity, efficiency, and beauty. The SVD principle resides in the decomposition of a matrix of arbitrary dimensions into the product of three matrices: $\mathbf{H}_{\mathrm{NTI}} = \mathbf{U}\ \mathbf{S}\ \mathbf{V}^t$, where $\mathbf{S}$ is a diagonal matrix whose diagonal elements (singular values) are either positive or zero and $\mathbf{U}^t\ \mathbf{U} = \mathbf{V}^t\ \mathbf{V} = 1$. A carefree inversion of $\mathbf{H}_{\mathrm{NTI}}$ gives

$$\begin{aligned} \mathbf{H}^{-1}_{\mathrm{NTI}} &= [\mathbf{U}\ \mathbf{S}\ \mathbf{V}^t]^{-1} \\ &= [\mathbf{V}^t]^{-1}\ \mathbf{S}^{-1}\ \mathbf{U}^{-1} \\ &= \mathbf{V}\ \mathbf{S}^{-1}\ \mathbf{U}^t, \end{aligned} \tag{9}$$

where the last line is obtained by using the orthonormal property of both $\mathbf{V}$ and $\mathbf{U}$. One advantage of SVD is to signal any problems by inserting zeros on the diagonal of $\mathbf{S}$. Since the degradation shows a loss of $N-1$ dimensions, we expect to find $N-1$ zero singular values (the dimension of $\mathbf{H}_{\mathrm{NTI}}$ is $MN \times MN + N - 1$, forcing the rank of $\mathbf{H}^{-1}$ to be MN). One commonly accepted means to compute $\mathbf{S}^{-1}$ is to let the zero singular values of $\mathbf{S}$ remain zero in $\mathbf{S}^{-1}$ while forcing the values that are small enough in $\mathbf{S}^{-1}$ to introduce some instability to zero in $\mathbf{S}^{-1}$. Press *et al.*[11] provide both an overview of the SVD method and an algorithm that generates $\mathbf{U}$, $\mathbf{S}$, and $\mathbf{V}$.

We conclude that the high-resolution restored vector signal $\hat{\mathbf{x}}^t_{\mathrm{NTI}}$ is obtained by multiplying $\mathbf{H}^{-1}$ by $\mathbf{z}_{\mathrm{NTI}}$.

5. EXAMPLES

To illustrate the results of the technique presented herein, we provide two examples, both of which start with artificially generated high-resolution vector signals.

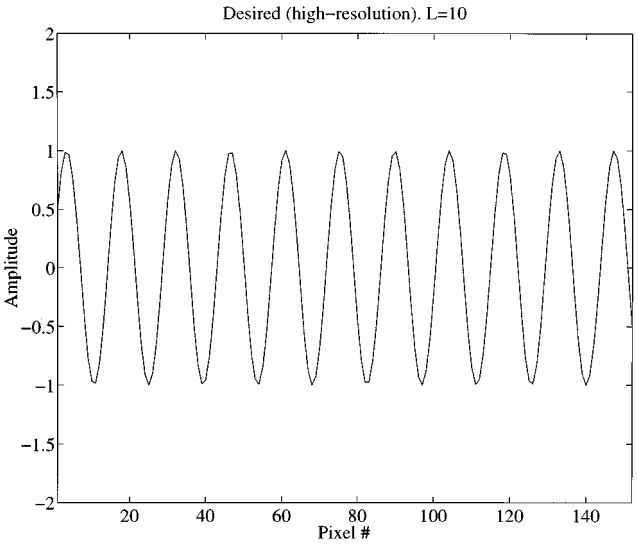

Fig. 3. Original high-resolution vector signal generated by Eq. (11).

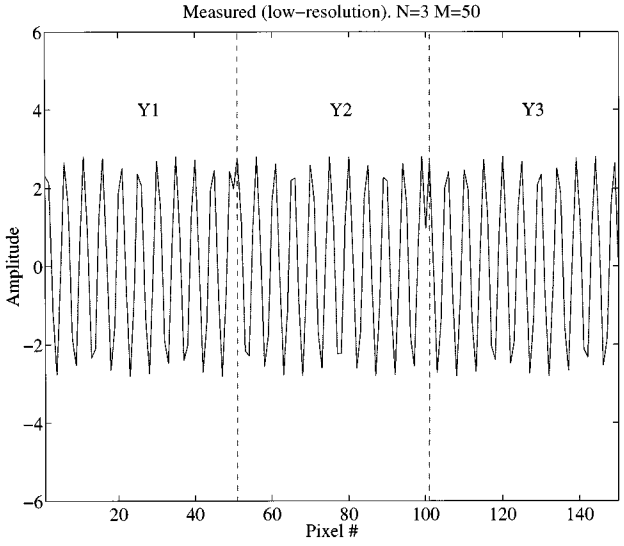

Fig. 4. Simulation of the recorded low-resolution signal as calculated by Eq. (2).

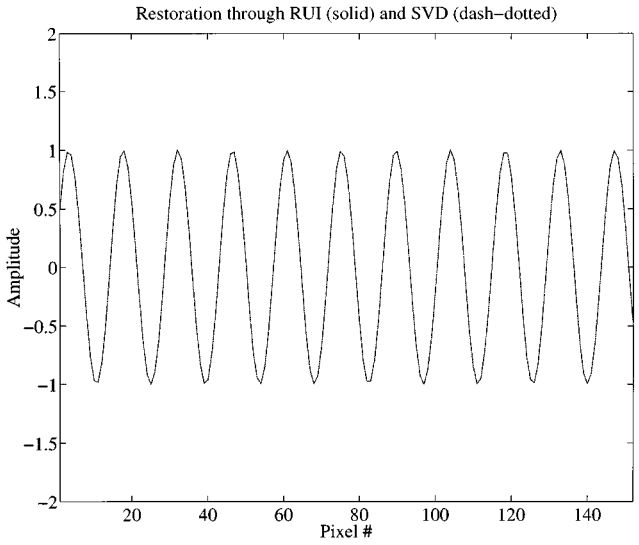

Fig. 5. Restoration through RUI and SVD of the low-resolution signal of Fig. 4. The two restorations overlap.

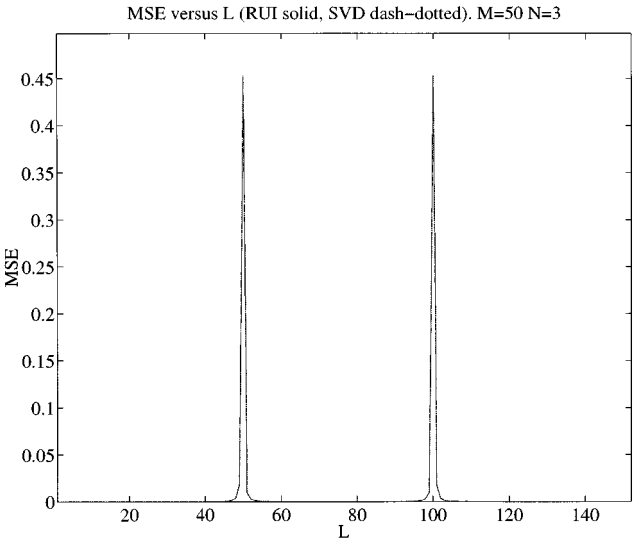

Fig. 6. Mean square error of the recovered signal (Fig. 5) and its high-resolution original (Fig. 3) as the frequency is changed (noiseless case). The curves for RUI and SVD overlap.

The degradation model first computes the low-resolution vector signal [Eq. (2)], followed by the noise addition [Eq. (1)]. Then the restoration model consists in the multiplication of the result of Eq. (1) by $\mathbf{H}^{-1}$ to obtain the estimated high-resolution vector signal. Comparison between the restored high-resolution vector signal and the original one is done by calculation of the MSE, whose expression is

$$\mathrm{MSE} = \frac{1}{MN + N - 1} \sum_{i=1}^{MN+N-1} [\hat{x}(i)_{\mathrm{NTI}} - x(i)_{\mathrm{original}}]^2 \tag{10}$$

for RUI and SVD reconstructions, both of which provide $MN + N - 1$ high-resolution pixels. Some figures use the SNR that is calculated for $\mathbf{z}$, the noisy low-resolution vector signal.

The first example is based on a sinusoidal wave whose equation is

$$x(k) = \sin\left[\frac{2\pi L + \phi_2 - \phi_1}{MN + N - 2}(k - 1) + \phi_1\right]$$
$$\phi_1 \in [0, \pi[,\ \phi_2 \in [\pi, 2\pi[,$$
$$k = 1, 2 \ldots MN + N - 1, \tag{11}$$

where L controls the number of full periods over the high-resolution vector signal, ϕ_1 is the desired phase when $k = 1$, and ϕ_2 is the desired phase modulo 2π when $k = MN + N - 1$. We arbitrarily chose $\phi_1 = \pi/6$ and $\phi_2 = \phi_1 + \pi$. Figures 3–5 exemplify a noiseless recovery through RUI and SVD, whose MSE's share the same value of 8.2×10^{-6} when $L = 10$, $M = 50$, and $N = 3$.

Figure 6 shows the frequencies for which the recovery is faulty, as explained by Eq. (6): this result is derivable

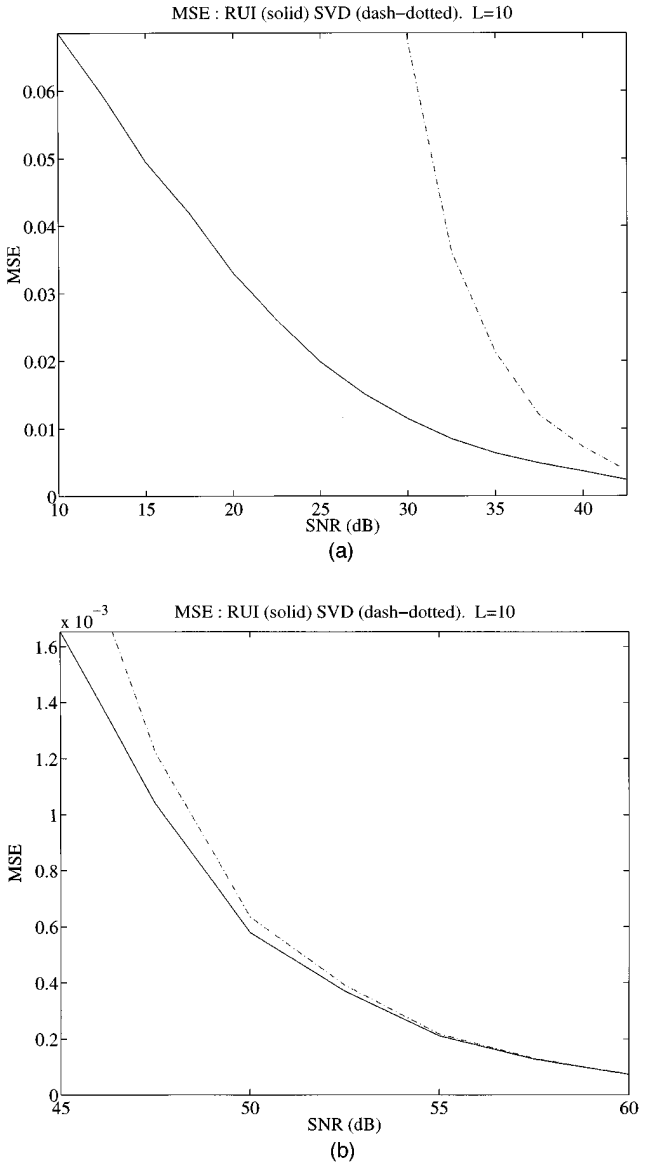

Fig. 7. Mean square error of both RUI and SVD recoveries of Fig. 3 as the SNR varies (a) from 10 to 43 dB and (b) from 45 to 60 dB. Solid curve, RUI; dashed–dotted curve, SVD. The constant C was set to 10 for the RUI restoration.

by solving $\Omega \times N/2 = n\pi$ for L while rejecting those for which $\Omega/2 = m\pi$, where both n and m are integer numbers and $\Omega = (2\pi L + \phi_2 - \phi_1)/(MN + N - 2)$. The SNR is given by the ratio of the average power of the low-resolution signal to the variance of the noise at the same location:

$$\mathrm{SNR}_{\mathrm{dB}} = 10 \log_{10}\left\{ \frac{1}{2{\sigma_n}^2} \left[\frac{\sin(N\Omega/2)}{\sin(\Omega/2)} \right]^2 \right\}, \qquad (12)$$

where ${\sigma_n}^2$ is the variance of the degraded noise [Brown and Hwang[5] provide a method for obtaining Eq. (12)]. Figure 7 plots MSE versus $\mathrm{SNR}_{\mathrm{dB}}$. As N is increased (keeping about the same dimension for the high-resolution vector signal) the number of frequencies that are not recoverable increases, therefore increasing the MSE. Hence the smaller N, the smaller the MSE for a given SNR. A plot addressing this point is presented

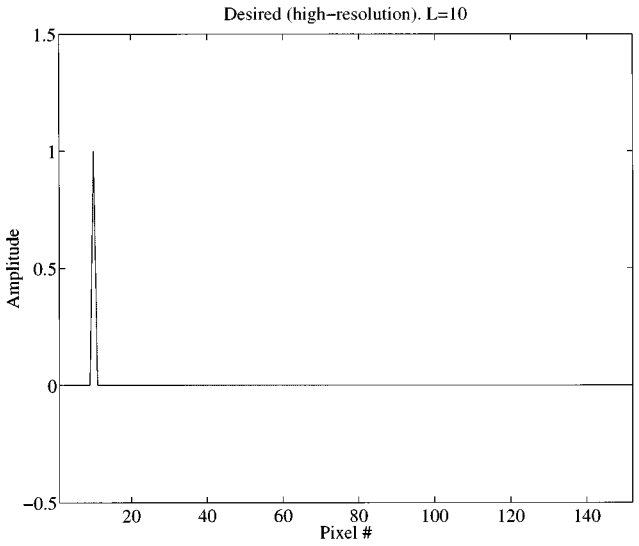

Fig. 8. Original high-resolution signal generated by Eq. (13).

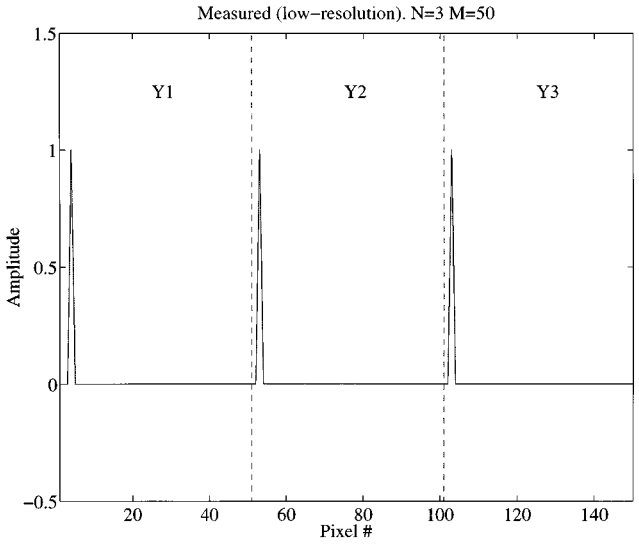

Fig. 9. Simulation of the recorded low-resolution signal as calculated by Eq. (2).

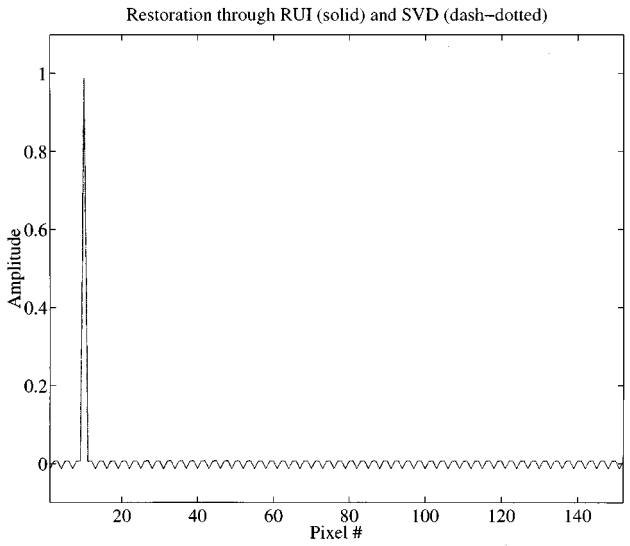

Fig. 10. Restoration through both RUI and SVD of the low-resolution vector signal (Fig. 9). The two curves overlap (noiseless case).

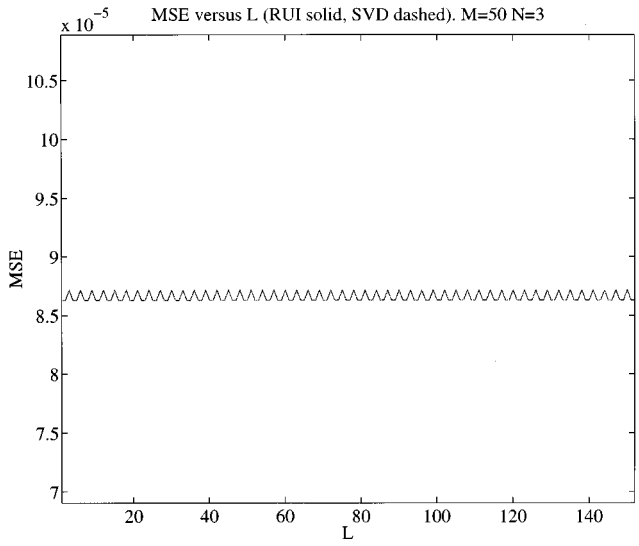

Fig. 11. Mean square error for the recoveries performed by both RUI and SVD. The curves overlap (noiseless case).

with the second example. If $x(k)$ is an undersampled version of $x(t)$, notice that the aliased form of $x(t)$ is recovered.

The second example is based on a periodic pulse of amplitude 1 whose period is $MN + N - 1$. Periodicity is required to obtain a nonzero SNR. Different locations are possible for this pulse within the high-resolution vector signal. The mathematical expression is

$$x(k) = \delta_{k,L} = \begin{cases} 1 & k = L \\ 0 & k \neq L, \end{cases} \qquad (13)$$

where $k = 1, 2 \ldots MN + N - 1$. Figure 8 shows the high-resolution signal for which $L = 10$, Fig. 9 plots the noiseless low-resolution vector signal, as it would be captured by an instrument when $M = 50$ and $N = 3$, and Fig. 10 displays the recovered results. The MSE for both RUI and SVD was 8.6×10^{-5} in the noiseless case. Notice, as shown in Figs. 10 and 11, that it is not possible to

perfectly recover the original high-resolution signal despite the total absence of noise. The SNR for the signal of interest is found to be

$$\mathrm{SNR}_{\mathrm{dB}} = 10 \log_{10}\left[\frac{N}{(MN + N - 1)\sigma_n{}^2}\right]. \qquad (14)$$

Figure 12 points out that the higher the SNR, the higher the quality of the restored image. Figure 13 shows that, as commented on in the first example, the MSE's of both the RUI and the SVD recoveries increase as the number of pulses N increases. This arises because not all frequencies provided by the Fourier transform of Eq. (13) are recoverable; the larger N, the higher the number of unrecoverable frequencies.

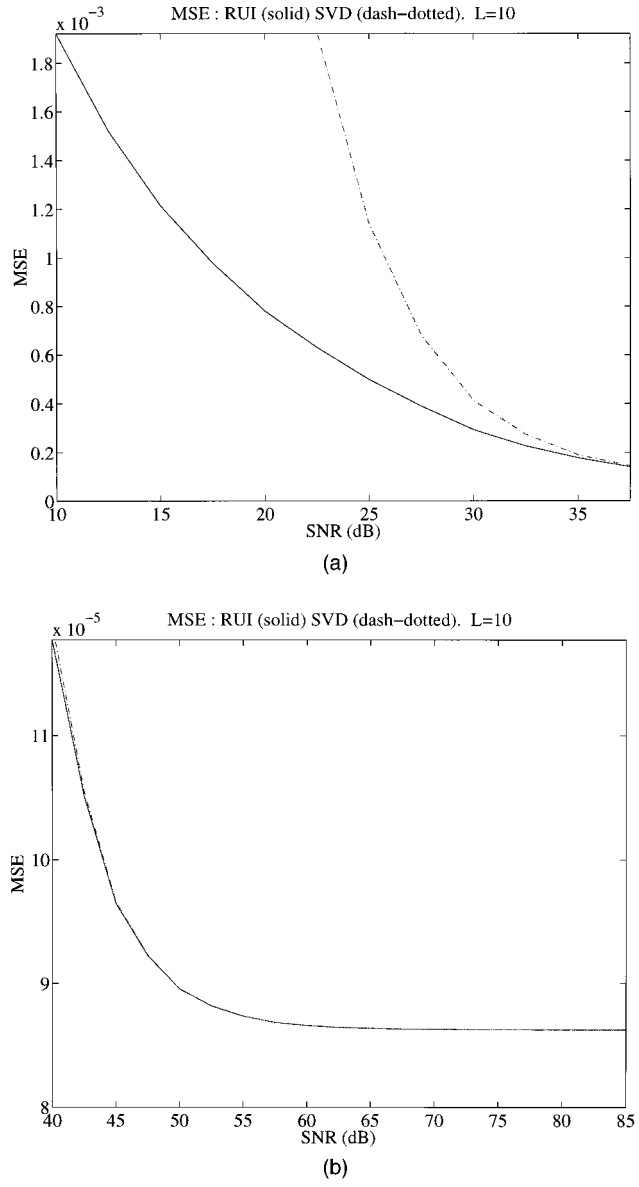

Fig. 12. Mean square error of both RUI and SVD recoveries of Fig. 8 as the SNR varies (a) from 10 to 38 dB and (b) from 40 to 85 dB. Solid curve, RUI; dashed–dotted curve, SVD. The constant C was set to 3 for the RUI restoration.

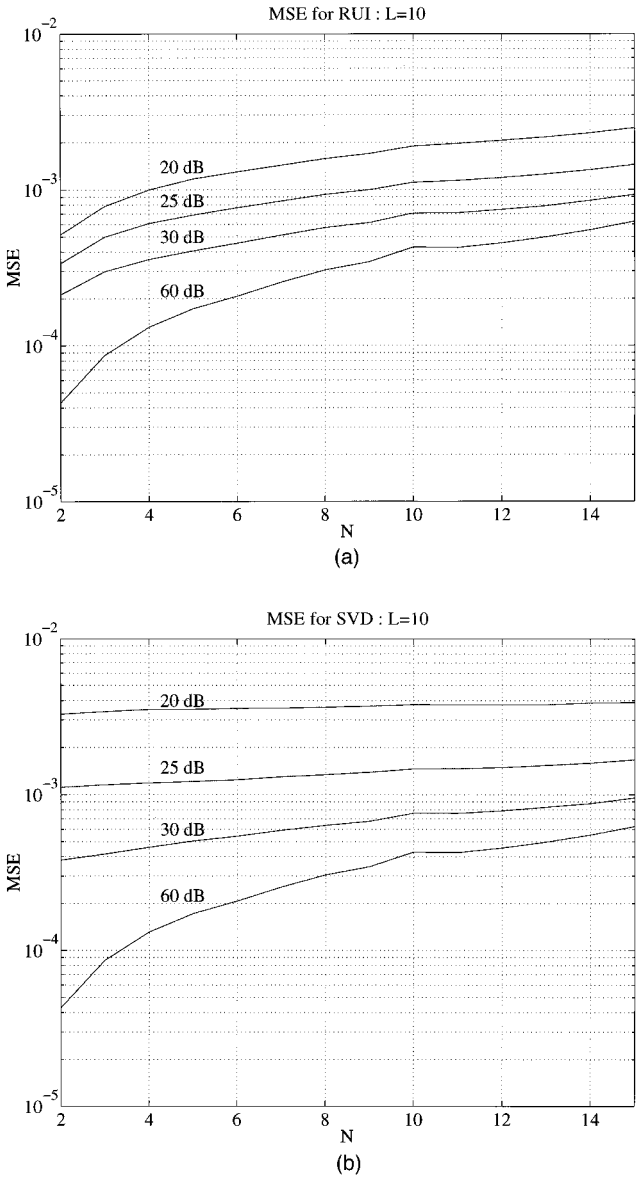

Fig. 13. Mean square error as both N and the SNR are varied for (a) the RUI recovery and (b) the SVD recovery. The length of the high-resolution signal was kept approximately constant. $M = 50$ when $N = 3$.

Both of the elementary examples provided in the present section, the choice of which is motivated by their ability to be a base to describe any signal, show that the essential characteristics of the recovery are strongly dependent on the selection of N, the SNR, and the associated restoration filter.

6. CONCLUSION

We have seen that a technique based on a series of time-shifted pulses allows for the procurement of a high-resolution vector signal (except for a few predictable unrecoverable frequencies) from a complete set of low-resolution vector signals. Two algorithms were compared: the regularized underconstrained inverse (RUI) and the singular value decomposition (SVD). The

former provided more robust answers when the SNR of the collected data was low, but the quality of the recovery it provided was comparable to that of SVD as the SNR increased to become significantly high.

We noticed that the smaller the number of low-resolution vector signals needed to make a complete set of measurements, the better. The dynamics of the probed environment, the frequencies of interest, and the availability of the hardware should also be considered.

One among the several applications this technique offers is an increase of accuracy in target ranging.

ACKNOWLEDGMENTS

The authors thank the reviewer for providing constructive suggestions. This research was supported in part by the Department of Electrical Engineering at The Pennsylvania State University and NASA grant NAG5-5035.

REFERENCES

1. M. K. Özkan, A. T. Erdem, M. I. Sezan, and A. M. Tekalp, "Efficient multiframe Wiener restoration of blurred and noisy image sequences," IEEE Trans. Image Process. **1**, 453–476 (1992).
2. A. N. Tikhonov and V. Y. Arsenin, *Solutions of Ill-posed Problems* (Wiley, New York, 1977).
3. M. Bertero, "Linear inverse and ill-posed problems," in *Advances in Electronics and Electron Physics*, Peter W. Hawkes, ed. (Academic, San Diego, Calif., 1989), Vol. 75.
4. R. C. Gonzalez and R. E. Woods, *Digital Image Processing* (Addison-Wesley, Reading, Mass., 1992).
5. R. G. Brown and P. Y. C. Hwang, *Introduction to Random Signals and Applied Kalman Filtering* (Wiley, New York, 1992).
6. A. Gelb, J. F. Kasper, Jr., R. A. Nash, Jr., C. F. Price, and A. A. Sutherland, *Applied Optimal Estimation* (MIT Press, Cambridge, Mass., 1974).
7. H. L. van Trees, Detection, *Estimation and Modulation Theory. Part I: Detection* (Wiley, New York, 1968).
8. R. M. Measures, *Laser Remote Sensing: Fundamentals and Applications* (Krieger, Malabar, Fla., 1992).
9. J. B. Abiss and B. J. Brames, "Restoration of sub-pixel detail using the regularized pseudo-inverse of the imaging operator," in *Advanced Signal Processing, Architectures and Implementations II*, F. T. Luk, ed., Proc. SPIE **1566**, 365–375 (1991).
10. G. Wahba, "Practical approximate solutions to linear operator equations when the data are noisy," SIAM J. Numer. Anal. **14**, 651–667 (1977).
11. W. H. Press, S. A. Teukolsky, W. T. Vetterling, and B. P. Flannery, *Numerical Recipes in C* (Cambridge U. Press, Cambridge, 1992).